CrossMark
click for updates

Spin Seebeck effect in insulating epitaxial γ−Fe₂O₃ thin films

P. Jiménez-Cavero,[1,2] I. Lucas,[1,2,3,a] A. Anadón,[1,2] R. Ramos,[4] T. Niizeki,[4]
M. H. Aguirre,[1,2,3,5] P. A. Algarabel,[2,6] K. Uchida,[7,8,9] M. R. Ibarra,[1,2,3,5]
E. Saitoh,[4,5,9,10] and L. Morellón[1,2,3]

[1]*Instituto de Nanociencia de Aragón, Universidad de Zaragoza, 50018 Zaragoza, Spain*
[2]*Departamento de Física de la Materia Condensada, Universidad de Zaragoza,
50009 Zaragoza, Spain*
[3]*Fundación INA, 50018 Zaragoza, Spain*
[4]*WPI Advanced Institute for Materials Research, Tohoku University, Sendai 980-8577, Japan*
[5]*Laboratorio de Microscopías Avanzadas, Universidad de Zaragoza, 50018 Zaragoza, Spain*
[6]*Instituto de Ciencia de Materiales de Aragón, Universidad de Zaragoza and Consejo Superior
de Investigaciones Científicas, E-50009 Zaragoza, Spain*
[7]*National Institute for Materials Science, Tsukuba 305-0047, Japan*
[8]*PRESTO, Japan Science and Technology Agency, Saitama 332-0012, Japan*
[9]*Institute for Materials Research, Tohoku University, Sendai 980-8577, Japan*
[10]*Advanced Science Research Center, Japan Atomic Energy Agency, Tokai 319-1195, Japan*

We report the fabrication of high crystal quality epitaxial thin films of maghemite (γ−Fe₂O₃), a classic ferrimagnetic insulating iron oxide. Spin Seebeck effect (SSE) measurements in γ−Fe₂O₃/Pt bilayers as a function of sample preparation conditions and temperature yield a SSE coefficient of 0.5(1) μV/K at room temperature. Dependence on temperature allows us to estimate the magnon diffusion length in maghemite to be in the range of tens of nanometers, in good agreement with that of conducting iron oxide magnetite (Fe₃O₄), establishing the relevance of spin currents of magnonic origin in magnetic iron oxides. *© 2017 Author(s). All article content, except where otherwise noted, is licensed under a Creative Commons Attribution (CC BY) license (http://creativecommons.org/licenses/by/4.0/).* [http://dx.doi.org/10.1063/1.4975618]

The study of correlations between spin and thermal currents has received much attention during the last decade, along with the designation of *spin caloritronics* or *thermospintronics*, and finally established as a field within the discipline of spintronics.[1] The report in 2008 of the first observation of Spin Seebeck effect (SSE) in permalloy films by Uchida *et al.* is usually pointed as the origin of the field.[2] Since then, publication of an increasing number of experimental works has triggered the appearance of a number of theoretical approaches to the phenomena.[3–7] The generation of a spin current on a ferromagnet (FM) subjected to a thermal gradient and detection through an attached non-magnetic (NM) layer—the Spin Seebeck effect—remains being one of the major results in the field. However, the underlying mechanisms contributing to the SSE have not been unambiguously elucidated yet.[8–12]

SSE is expected to bring a considerable improvement in the performance of thermoelectric devices in energy harvesting applications, and also constitutes a novel alternative for the generation of spin currents in spintronic devices.[13–15] In this regard, testing the SSE performance of iron oxides, which are the magnetic materials known since long, is worthwhile. Results have already been reported for epitaxial thin films of inverse spinel Fe₃O₄ (magnetite).[16,17] However, its conducting behavior ensues two problems for the study of SSE in this material. On the one hand, SSE experiments are performed most often in the so-called longitudinal configuration (LSSE).[13,18] In this geometry, the FM/NM interface and magnetic field are parallel between them and perpendicular to the thermal gradient and the spin current, as depicted in Fig. 1(a); this is the same geometry in which another

---
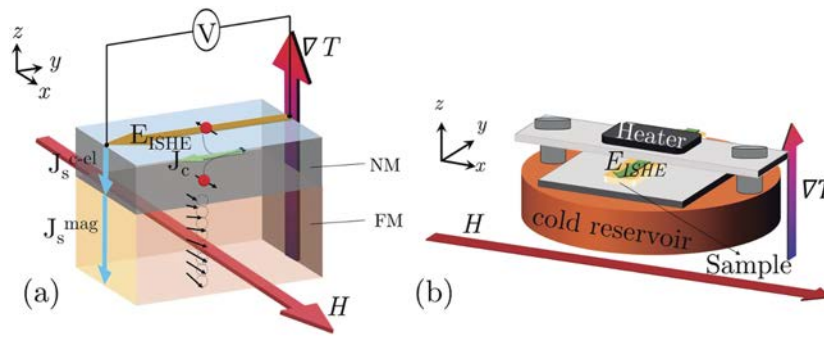
[a]ilucas@unizar.es

5, 026103-1

FIG. 1. Geometry schemes of the LSSE experiment (a) and the experimental setup (b).

thermospintronic effect arises in metallic materials with itinerant electrons: the Anomalous Nernst Effect (ANE), which generates a voltage $V_{ANE} \propto \mathbf{M} \times \nabla T$. Therefore, both signals are expected to be superimposed.[19] The other issue is more fundamental: most theoretical models rely on the generation of magnonic spin current in the FM ($\mathbf{J}_S^{mag}$) and its injection by spin pumping into the NM, where it is carried by itinerant electrons ($\mathbf{J}_S^{c\text{-}el}$).[3–5,7] This spin current is often detected by its conversion in charge current due to Inverse Spin Hall effect (ISHE) in an attached metallic layer, usually Pt due to its high ISHE efficiency.[20] These models do not consider a possible contribution from a conduction-electron spin current that might be excited in a conductive ferromagnet, such as magnetite, by the thermal gradient. This may question the validity of these models to the study of SSE in magnetite.

In contrast to magnetite, iron oxide maghemite $\gamma-Fe_2O_3$ is an insulator with a band gap of $\sim$2.0 eV.[21] The mechanism for conduction in magnetite is believed to be the hopping of electrons between Fe^{3+} and Fe^{2+}; in the case of maghemite, only the trivalent state of iron is present, resulting in the insulating behavior. The crystal structure of $\gamma-Fe_2O_3$ is similar to that of Fe_3O_4: an inverse spinel.[21,22] Since in this case both tetrahedral and octahedral sites are occupied by Fe^{3+} cations, charge neutrality in the cell is kept by the presence of cation vacancies in the octahedral positions. The unit cell of maghemite could therefore be written as $(Fe^{3+})_8[Fe_{5/6}^{3+}\otimes_{1/6}]_{16}O_{32}^{2-}$, where ( ) denotes the tetrahedral sites and [ ] the octahedral ones: 8/3 vacancies are created out of the 24 Fe^{3+} sites within the cell.[21] These vacancies can be either randomly distributed within the crystal, or follow an ordered pattern; in this case, a tetragonal superstructure keeping $c = 3a$ arises (see the supplementary material), with a and c being the in- and out-of-plane lattice parameters, respectively.[21,23] $\gamma-Fe_2O_3$ also shows ferrimagnetic behavior with magnetic saturation similar to Fe_3O_4, around 400 emu/cm,[3] and slightly higher Néel temperature $\sim$900 K. All in all, $\gamma-Fe_2O_3$ stands as a good candidate to be tested in SSE devices: not only is it a reasonably well known magnetic and insulating material, already used in magnetic recording technologies,[24] but also, given the similarity in structure, composition, and magnetic properties between maghemite and magnetite, it could help to validate or refute the application of magnonic spin current models for the SSE in the latter.

In this paper, we report the preparation and characterization of epitaxial $\gamma-Fe_2O_3$ thin films and the result of SSE measurements depending on some growth conditions. We also compare the SSE output of maghemite and magnetite. SSE experiments were performed in the longitudinal configuration sketched in Fig. 1. It is important to note that, due to $\gamma-Fe_2O_3$ insulating behavior, no ANE signal will contaminate the output voltage. The used experimental setup is depicted in Fig. 1(b): the sample is placed between two AlN plates and the thermal gradient in the z direction is generated by the application of an electric current to a resistive heater placed on the upper plate. The temperature at the lower and upper plates is monitored by two T-type thermocouples. The electrical contacts were made using Al wires with 25 μm diameter, and the output signal V_y is recorded using a Keithley 2182A nanovoltmeter.

Samples were prepared following a three-step procedure: first, pulsed laser deposition (PLD) was used to deposit layers from a 99.9% pure Fe_3O_4 target in high vacuum conditions. The base pressure in the deposition chamber was $\sim10^{-8}$ Torr. Second, Fe_3O_4 films were subsequently *in situ* annealed

in oxygen atmosphere at 325 °C to obtain the $\gamma-Fe_2O_3$ phase. Finally, the Pt detecting layer was *in situ* sputtered at room temperature, in the case of samples to be used in SSE experiments. Repetition rate of the KrF excimer 248 nm wavelength laser was set to 10 Hz with 3×10^9 W/cm^2 irradiance. Partial oxygen pressures during annealing were varied in a range from 1 mTorr to 100 mTorr in order to find the optimal value, attending to the structural and magnetic characterization. Concerning annealing duration, we found that 2.5 h were enough to accomplish the full oxidation of the films (see the supplementary material). Samples were kept in the same chamber during all the processes. The thickness of the samples was determined by X-ray reflectivity (XRR) and by transmission electron microscopy (TEM) for films covered with Pt. All sample thicknesses are ~60 nm. Alternatively, we also prepared maghemite thin films using a different physical vapor deposition method (sputtering), to assess universality of the process. Characterization and results of the SSE experiments in the thus fabricated samples are compiled in the supplementary material.

Since $\gamma-Fe_2O_3$ phase was achieved by oxidation from Fe_3O_4, we must ensure not only that the whole sample underwent the phase transformation but also that the obtained phase is the desired $\gamma-Fe_2O_3$ rather than the more stable α-Fe_2O_3.[21,25,26] We did this by structural characterization using X-ray diffraction (XRD), electron diffraction in TEM, and X-ray photoelectron spectroscopy (XPS). Magnetic characterization also allows to rule out the presence of α-Fe_2O_3, since its antiferromagnetic behavior would considerably decrease the magnetic signal. In addition, the absence of the Verwey transition would be a good indication, although not definitive, of the transformation of the Fe_3O_4 phase. Only after careful determination of the phases present in the sample depending on the growth condition, we will proceed to the SSE experiments.

The crystalline structure was studied by XRD in a Bruker D8 Advance High resolution diffractometer. The $2\theta/\omega$ pattern in the symmetric configuration shows a shift of the film peak with respect to the Fe_3O_4, as shown in Fig. 2. For epitaxial Fe_3O_4 thin films, diffraction occurs at $2\theta = 43.19°$, whereas the peak of annealed films is observed at $2\theta \sim 43.82°$. This value is very close to the expected one considering a pure elastic, unit cell volume conserving deformation of epitaxially strained $\gamma-Fe_2O_3$ thin film on MgO substrate (vertical line in Fig. 2). Laue oscillations point out the existence of crystalline coherence along the whole thickness of the film.

XPS measurements at the Fe 2p energy edge allow to determine the oxidation state of Fe cations. We performed XPS analysis in samples prepared using different annealing pressures ranging from 0 (no annealing, pure magnetite) to 100 mTorr, using a Kratos AXIS Ultra DLD spectrometer with Al Kα source. We used the C1s binding energy of C at 284.9 eV for calibration. The results are reported in Fig. 3, within the survey range of binding energies of the Fe 2p electrons (700 to 740 eV). In the case of pure magnetite films (Fig. 3(a)), we only see the Fe $2p_{1/2}$ and $2p_{3/2}$ main peaks. We fit the $2p_{3/2}$ peak to the conventional multiplet structure calculated by Gupta and Sen,[27] which allows us to estimate the stoichiometry of the sample and determine the parameters of the peak.[28] The binding
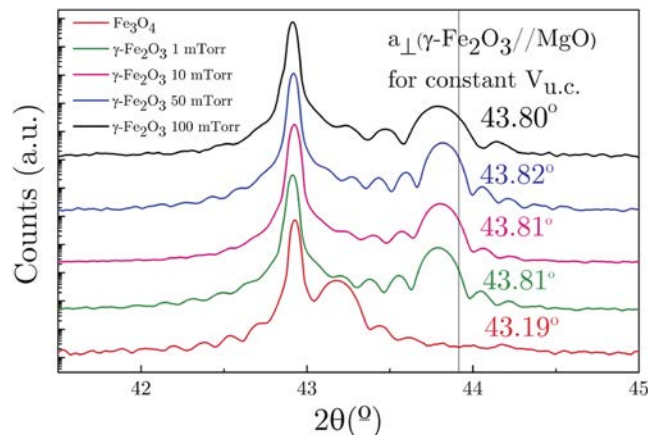

FIG. 2. X-ray diffraction patterns in the symmetric configuration around the (002) and (004) reflections for MgO and gamma-Fe_2O_3, respectively. The results are shown for samples prepared using different annealing pressures.
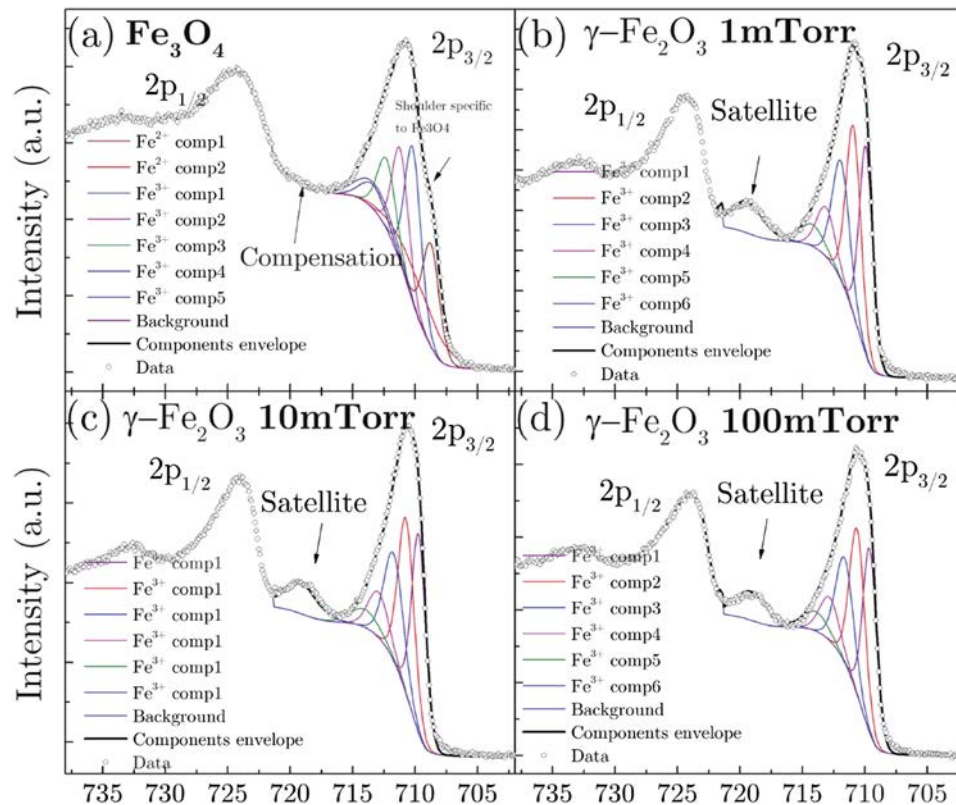
FIG. 3. (a) XPS spectrum of a reference magnetite. (b)–(d) XPS spectra of samples prepared with different annealing oxygen partial pressures.

energy is 710.8 eV, with the FWMH ~4.3 eV; these values are consistent with those reported for magnetite.[29,30] Fe:O ratio extracted from the fitting is 0.72(7). For the rest of the samples, all of which have been annealed, XPS spectra around Fe 2p show not only both main peaks but also a satellite structure at higher binding energies, which appears when only Fe^{3+} is present. In the case of pure magnetite, Fe^{3+} and Fe^{2+} satellite structures compensate each other and no satellite accompanies the main $2p_{1/2}$ and $2p_{3/2}$ peaks.[30] The distance between the satellite and the main Fe $2p_{3/2}$ peak is $\Delta \sim 8.0$ eV for all annealed samples, agreeing with previous reports for $\gamma-Fe_2O_3$.[30–32] Apart from this main feature, there are other differences with respect to the magnetite reference sample: a shift of the binding energy to 711.1 eV and a narrowing of the peak down to FWMH ~3.0 eV, which are characteristic values for Fe^{3+},[30,31] thus entailing the absence of Fe_3O_4 phase. Finally, quantification yields Fe/O ~0.64(6).

Imaging and electron diffraction in a TEM can also help to differentiate the phases present in a sample. In Fig. 4, we present the diffraction pattern and High Angle Annular Dark Field Scanning TEM (HAADF-STEM) images for the reference magnetite (Figs. 4(a) and 4(b)) and for some of the annealed samples. The annealed samples show a different short range order structure; this order is represented by the diffraction spots $\pm(011)$ and $\pm(01\bar{1})$ that are permitted in the diffraction pattern of maghemite spinel but not in the magnetite spinel. Electron diffraction and TEM images also allow us to differentiate whether Fe vacancies are ordered or not (see the supplementary material). All samples used for SSE experiments showed the ordered pattern, which has been calculated to be the most thermodynamically stable configuration.[23]

Magnetic properties were characterized through in-plane $M(H)$ and $M(T)$ measurements performed in a SQUID magnetometer. In Figures 5(a) and 5(b) we compare the results for a Fe_3O_4 film and three annealed samples, at 1, 10, and 100 mTorr, respectively. We observe no reduction in saturation magnetization in any of the annealed samples, meaning that they are free from antiferromagnetic α-Fe_2O_3 phase.[25] In all cases, $M_S \sim 400$ emu/cm,[3] which is a typical value for both
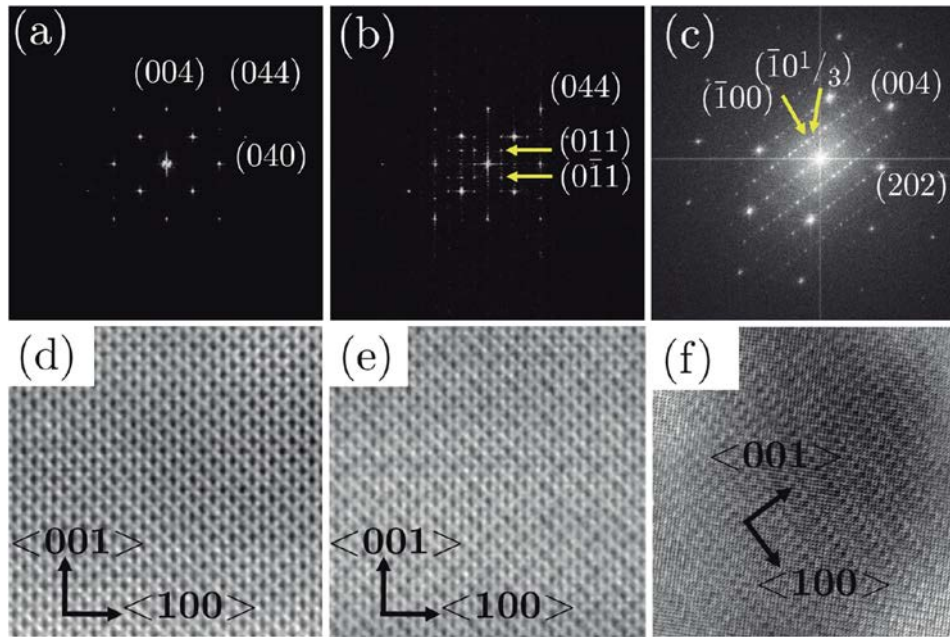
FIG. 4. (a) Electron diffraction pattern of the reference Fe_3O_4. (b) Electron diffraction pattern of one annealed sample, showing spots $\pm(011)$ and $\pm(01\bar{1})$. This specimen shows the disordered configuration of vacancies. (c) Electron diffraction pattern of one annealed sample, with the superstructure along c axis, due to an ordering of the vacancies. (d)–(f) HAADF-STEM images corresponding to the diffraction patterns above.

magnetite and maghemite films.[25,32,33] Coercivity of the annealed samples is slightly wider than for reference magnetite, as it is reported for maghemite.[32,34] As to $M(T)$ measurements in the presence of low magnetic field, the Fe_3O_4 reference sample shows a sharp Verwey transition with transition temperature $T_V \sim 115$ K. This transition vanishes for the annealed samples, meaning that the Fe_3O_4 phase has been removed, in agreement with XRD and TEM results.

The main differences between behaviors for different annealing pressures are found in the electrical characterization of samples. At room temperature, magnetite is a poor conductor with a reported resistivity of about 5×10^{-3} Ω·cm. We measured room temperature resistivity of the annealed films by the four-probe method. Resistivity of samples that were annealed under pressures $P \geq 10$ mTorr is beyond the range of our measurement system: 50 kΩ·cm for the dimensions of our films.

So far we have verified that we can produce $\gamma-Fe_2O_3$ showing good crystalline, magnetic, and electrical properties, free from other iron oxide phases. In the following we will show the SSE measurement results. The output V_y signal is separated in antisymmetric and symmetric components. The LSSE signal detected by ISHE is purely antisymmetric in field; any superimposed symmetric component is not to be attributed to the effect under study, and has been subtracted. An antisymmetric signal at saturating field, $\Delta V = V_y^{antisym} = \frac{1}{2}[V_y(+H_S) - V_y(-H_S)]$, is plotted against the thermal gradient and fitted to a linear dependence to obtain $\Delta V/\Delta T$ for each sample. The SSE signal is depicted in Fig. 5(c) for different annealing pressures, along with the scaling of the SSE signal with magnetization in Fig. 5(d). In the inset in Fig. 5(a) we see the value of SSE coefficient (SSC) for different annealing pressures, also in comparison to the SSC of magnetite. SSC has been defined as

$$SSC = \frac{\Delta V}{\Delta T}\frac{L_z}{L_y} = -\frac{E_y}{\nabla T}.$$

The 10 mTorr-annealed sample is quite similar to magnetite SSC, and it remains almost constant for higher annealing pressures, yielding SSC $= 0.5(1)$ μV/K. Given the similarity between $\gamma-Fe_2O_3$ and Fe_3O_4 structures and magnetic signal, this result suggests that spin current excited in magnetite and maghemite by SSE must be carried by the same mechanism: magnons rather than conduction
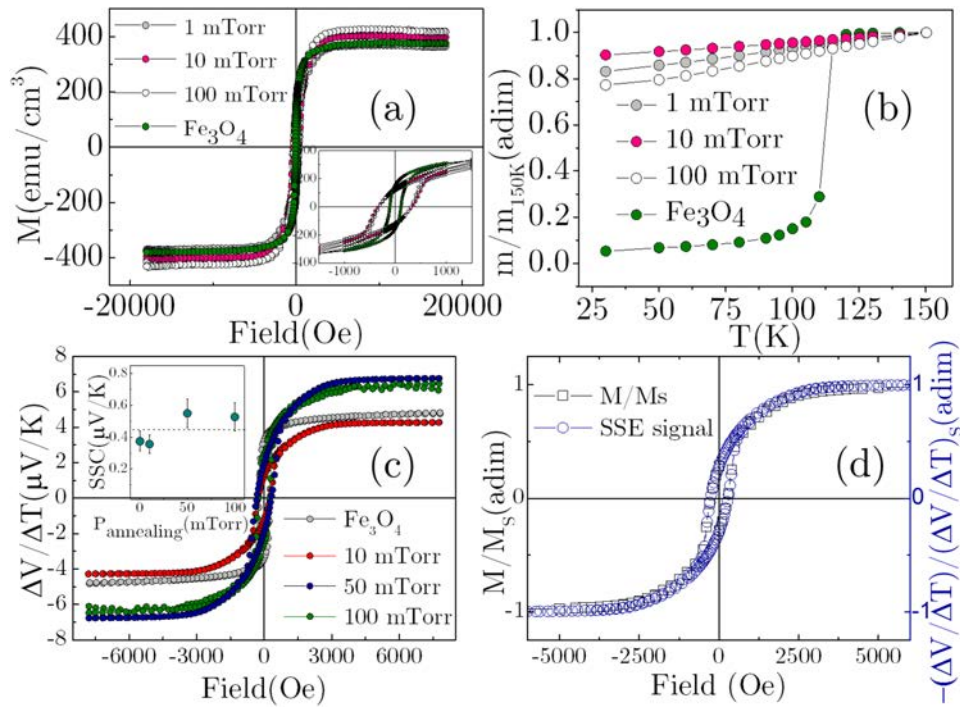
FIG. 5. (a) Hysteresis loops of samples prepared with different annealing oxygen partial pressures. The inset shows a zoom of the low field region. (b) Magnetization vs temperature behavior of samples, measured in the presence of low external field (500 Oe). The Fe_3O_4 reference sample clearly undergoes the Verwey transition. (c) SSE signal at $T = 300$ K for samples annealed at different pressures. Cycles were measured using $\Delta T = 1$ K. Inset: SSC obtained from measurements at $T = 300$ K under several thermal gradients. (d) Scaling of SSE and magnetic signals, corresponding to a sample annealed at oxygen partial pressure $P_{O_2}^{ann} = 10$ mTorr.

electrons, since maghemite is an insulator. Therefore, application of SSE theories relying only on magnonic spin currents to understand the experiments in magnetite seems legitimate.[4,7,17]

We finally measured the SSC dependence on the temperature of the sample prepared using annealing oxygen partial pressure $P_{O_2}^{ann} = 10$ mTorr. SSE dependence on temperature brings up fundamental issues about the mechanisms controlling the effect. The behavior of SSC when decreasing the temperature below room conditions has been reported to feature a peak in the case of experiments using YIG;[7,11,35] this peak is explained in terms of the competition between magnon propagation length, which increases when decreasing the temperature, and thermal magnon population, which decreases with decreasing the temperature. When the thickness of the sample becomes comparable
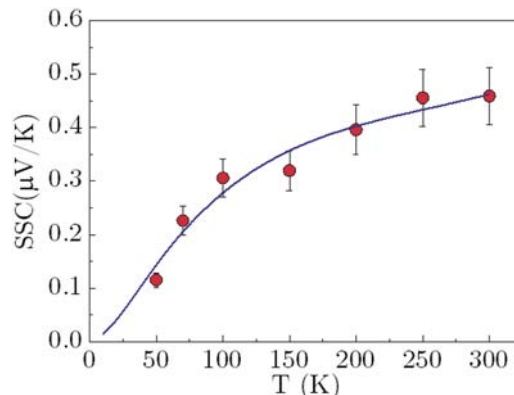

FIG. 6. Experimental data for SSC dependence with temperature. Blue line is intended as a guide to the eye.

to the magnon diffusion length (around a hundred nm in YIG[8]), the peak vanishes.[7,11] Our results for $\gamma-Fe_2O_3$ are plotted in Fig. 6, in which we observe no visible peak but rather a monotonic decrease, suggesting that reduction of magnon population is dominant over the increase in magnon propagation length. This behavior points out that magnon diffusion length in maghemite must be in the same order of magnitude of the thickness of our sample: tens of nanometers. This result is also in the range of the reported magnon diffusion length in magnetite.[36]

In conclusion, we have prepared epitaxial thin films of $\gamma-Fe_2O_3$, with no presence of other iron oxide phases, and good crystalline, magnetic, and electrical properties. We have performed LSSE experiments on the films and compared the results with those of conductive Fe_3O_4, finding no significant differences. This result suggests that the magnonic origin of the spin current in magnetite is a good approximation, consequently supporting the validity of the current models already proposed.[17] We have finally measured the temperature dependence of SSE in maghemite finding that it is in qualitative agreement with previous reports for other purely magnonic systems.

See supplementary material for details about the structure of $\gamma-Fe_2O_3$. We also show SSE results for maghemite thin films fabricated using a different physical vapor deposition method to demonstrate the universality of the process.

[1] G. E. W. Bauer, E. Saitoh, and B. J. van Wees, "Spin caloritronics," Nat. Mater. **11**, 391–399 (2012).

[2] K. Uchida, S. Takahashi, K. Harii, J. Ieda, W. Koshibae, K. Ando, S. Maekawa, and E. Saitoh, "Observation of the spin Seebeck effect," Nature **455**, 778–781 (2008).

[3] J. Xiao, G. E. W. Bauer, K. Uchida, E. Saitoh, and S. Maekawa, "Theory of magnon-driven spin Seebeck effect," Phys. Rev. B **81**(21), 214418 (2010).

[4] H. Adachi, K. Uchida, E. Saitoh, and S. Maekawa, "Theory of the spin Seebeck effect," Rep. Prog. Phys. **76**, 036501 (2013).

[5] S. Hoffman, K. Sato, and Y. Tserkovnyak, "Landau-Lifshitz theory of the longitudinal spin Seebeck effect," Phys. Rev. B **88**(6), 064408 (2013).

[6] S. M. Rezende, R. L. Rodríguez-Suárez, R. O. Cunha, A. R. Rodrigues, F. L. A. Machado, G. A. Fonseca Guerra, J. C. Lopez Ortiz, and A. Azevedo, "Magnon spin-current theory for the longitudinal spin-Seebeck effect," Phys. Rev. B **89**(1), 014416 (2014).

[7] S. M. Rezende, R. L. Rodríguez-Suárez, R. O. Cunha, J. C. López Ortiz, and A. Azevedo, "Bulk magnon spin current theory for the longitudinal spin Seebeck effect," J. Magn. Magn. Mater. **400**, 171–177 (2016).

[8] A. Kehlberger, U. Ritzmann, D. Hinzke, E. J. Guo, J. Cramer, G. Jakob, M. C. Onbasli, D. H. Kim, C. A. Ross, M. B. Jungfleisch, B. Hillebrands, U. Nowak, and M. Kläui, "Length scale of the spin Seebeck effect," Phys. Rev. Lett. **115**(9), 096602 (2015).

[9] J. D. Arboleda, O. Arnache Olmos, M. H. Aguirre, R. Ramos, A. Anadón, and M. R. Ibarra, "Spin Seebeck effect in a weak ferromagnet," Appl. Phys. Lett. **108**(23), 232401 (2016).

[10] S. M. Wu, J. E. Pearson, and A. Bhattacharya, "Paramagnetic spin Seebeck effect," Phys. Rev. Lett. **114**(18), 186602 (2015).

[11] E.-J. Guo, J. Cramer, A. Kehlberger, C. A. Ferguson, D. A. MacLaren, G. Jakob, and M. Kläui, "Influence of thickness and interface on the low-temperature enhancement of the spin seebeck effect in YIG films," Phys. Rev. X **6**(3), 031012 (2016).

[12] S. Geprägs, A. Kehlberger, F. D. Coletta, Z. Qiu, E.-J. Guo, T. Schulz, C. Mix, S. Meyer, A. Kamra, M. Althammer, H. Huebl, G. Jakob, Y. Ohnuma, H. Adachi, J. Barker, S. Maekawa, G. E. W. Bauer, E. Saitoh, R. Gross, S. T. B. Goennenwein, and M. Kläui, "Origin of the spin Seebeck effect in compensated ferrimagnets," Nat. Commun. **7**, 10452 (2016).

[13] K. Uchida, M. Ishida, T. Kikkawa, A. Kirihara, T. Murakami, and E. Saitoh, "Longitudinal spin Seebeck effect: From fundamentals to applications," J. Phys. Condens. Matter **26**, 343202 (2014).

[14] R. Ramos, A. Anadon, I. Lucas, K. Uchida, P. A. Algarabel, L. Morellon, M. H. Aguirre, E. Saitoh, and M. R. Ibarra, "Thermoelectric performance of spin Seebeck effect in Fe_3O_4/Pt-based thin film heterostructures," APL Mater. **4**(10), 104802 (2016).

[15] K. Uchida, H. Adachi, T. Kikkawa, A. Kirihara, M. Ishida, S. Yorozu, S. Maekawa, and E. Saitoh, "Thermoelectric generation based on spin Seebeck effects," Proc. IEEE **104**(10), 1946 (2016).

[16] R. Ramos, T. Kikkawa, K. Uchida, H. Adachi, I. Lucas, M. H. Aguirre, P. Algarabel, L. Morellón, S. Maekawa, E. Saitoh, and M. R. Ibarra, "Observation of the spin Seebeck effect in epitaxial Fe_3O_4 thin films," Appl. Phys. Lett. **102**(7), 072413 (2013).

[17] R. Ramos, T. Kikkawa, M. H. Aguirre, I. Lucas, A. Anadón, T. Oyake, K. Uchida, H. Adachi, J. Shiomi, P. A. Algarabel, L. Morellón, S. Maekawa, E. Saitoh, and M. R. Ibarra, "Unconventional scaling and significant enhancement of the spin Seebeck effect in multilayers," Phys. Rev. B **92**(22), 220407 (2015).

[18] K. Uchida, H. Adachi, T. Ota, H. Nakayama, S. Maekawa, and E. Saitoh, "Observation of longitudinal spin-Seebeck effect in magnetic insulators," Appl. Phys. Lett. **97**(17), 172505 (2010).

[19] R. Ramos, M. H. Aguirre, A. Anadón, J. Blasco, I. Lucas, K. Uchida, P. A. Algarabel, L. Morellón, E. Saitoh, and M. R. Ibarra, "Anomalous Nernst effect of Fe_3O_4 single crystal," Phys. Rev. B **90**(5), 054422 (2014).

[20] A. Hoffmann, "Spin Hall effects in metals," IEEE Trans. Magn. **49**(10), 5172 (2013).

[21] R. Grau-Crespo, A. Y. Al-Baitai, I. Saadoune, and N. H. De Leeuw, "Vacancy ordering and electronic structure of γ -Fe_2O_3 (maghemite): A theoretical investigation," J. Phys. Condens. Matter **22**, 255401 (2010).

[22] L. MacHala, J. Tuček, and R. Zbořil, "Polymorphous transformations of nanometric iron(III) oxide: A review," Chem. Mater. **23**, 3255 (2011).

[23] H. Yanagihara, M. Hasegawa, and E. Kita, "Iron vacancy ordered γ–Fe_2O_3 (001) epitaxial films: The crystal structure and electrical resistivity," J. Phys. Soc. Jpn. **75**(5), 054708 (2006).

[24] R. Dronskowski, "The little maghemite story: A classic functional material," Adv. Funct. Mater. **11**(1), 27 (2001).

[25] X. L. Huang, Y. Yang, and J. Ding, "Epitaxial growth of c-Fe_2O_3 thin films on MgO substrates by pulsed laser deposition and their properties," Acta Mater. **61**, 548 (2013).

[26] A. M. Jubb and H. C. Allen, "Vibrational spectroscopic characterization of hematite, maghemite, and magnetite thin films produced by vapor deposition," ACS Appl. Mater. Interfaces **2**(10), 2804 (2010).

[27] R. P. Gupta and S. K. Sen, "Calculation of multiplet structure of core p-vacancy levels," Phys. Rev. B **12**(1), 15 (1975).

[28] M. C. Biesinger, B. P. Payne, A. P. Grosvenor, L. W. M. Lau, A. R. Gerson, and R. St. C. Smart, "Resolving surface chemical states in XPS analysis of first row transition metals, oxides and hydroxides: Cr, Mn, Fe, Co and Ni," Appl. Surf. Sci. **257**, 2717 (2011).

[29] S. Gota, E. Guiot, M. Henriot, and M. Gautier-Soyer, "Atomic-oxygen-assisted MBE growth of α-Fe_2O_3 on α-Al_2O_3(0001): Metastable FeO(111)-like phase at subnanometer thicknesses," Phys. Rev. B **60**(20), 14387 (1999).

[30] T. Yamashita and P. Hayes, "Analysis of XPS spectra of Fe^{2+} and Fe^{3+} ions in oxide materials," Appl. Surf. Sci. **254**, 2441 (2008).

[31] A. Fujimori, M. Saeki, N. Kimizuka, M. Taniguchi, and S. Suga, "Photoemission satellites and electronic structure of Fe_2O_3," Phys. Rev. B **34**(10), 7318 (1986).

[32] P. Li, E. Y. Jiang, and H. L. Bai, "Fabrication of ultrathin epitaxial γ-Fe_2O_3 films by reactive sputtering," J. Phys. D. Appl. Phys. **44**, 075003 (2011).

[33] A. Espinosa, A. Serrano, A. Llavona, J. Jimenez de la Morena, M. Abuin, A. Figuerola, T. Pellegrino, J. F. Fernández, M. Garcia-Hernandez, G. R. Castro, and M. A. Garcia, "On the discrimination between magnetite and maghemite by XANES measurements in fluorescence mode," Meas. Sci. Technol. **23**, 015602 (2012).

[34] T. Tepper, C. A. Ross, and G. F. Dionne, "Microstructure and optical properties of pulsed-laser-deposited iron oxide films," IEEE Trans. Magn. **40**(3), 1685 (2004).

[35] T. Kikkawa, K. Uchida, S. Daimon, Z. Qiu, E. Shiomi, and Y. Saitoh, "Critical suppression of spin Seebeck effect by magnetic fields," Phys. Rev. B **92**(6), 064413 (2015).

[36] A. Anadón, R. Ramos, I. Lucas, P. A. Algarable, L. Morellón, M. R. Ibarra, and M. H. Aguirre, "Characteristic length scale of the magnon accumulation in Fe_3O_4/Pt bilayer structures," Appl. Phys. Lett. **109**(1), 012404 (2016).